DOI: 10.1007/s11661-007-9167-9
© The Minerals, Metals & Materials Society and ASM International 2007

Microstructural Evolution During Laser Resolidification of Fe-25 Atom Percent Ge Alloy

KRISHANU BISWAS and KAMANIO CHATTOPADHYAY

The microstructural evolution of concentrated alloys is relatively less understood both in terms of experiments as well as theory. Laser resolidification represents a powerful technique to study the solidification behavior under controlled growth conditions. This technique has been utilized in the current study to probe experimentally microstructural selection during rapid solidification of concentrated Fe-25 atom pct Ge alloy. Under the equilibrium solidification condition, the alloy undergoes a peritectic reaction between ordered α_2 (B2) and its liquid, leading to the formation of ordered hexagonal intermetallic phase ε (DO_{19}). In general, the as-cast microstructure consists of ε phase and ε–β eutectic and α_2 that forms as a result of an incomplete peritectic reaction. With increasing laser scanning velocity, the solidification front undergoes a number of morphological transitions leading to the selection of the microstructure corresponding to metastable α_2/β eutectic to α_2 dendrite + α_2/β eutectic to α_2 dendrite. The transition velocities as obtained from the experiments are well characterized. The microstructural selection is discussed using competitive growth kinetics.

I. INTRODUCTION

TECHNIQUES of rapidly melting and subsequent cooling of the surface of a material using high-power laser or electron beams offer a unique way of achieving rapid solidification. In the case of laser resolidification, which usually involves solidification at high rates (as high as 18 ms^{-1}[1]), the conditions of equilibrium at the moving solid–liquid interface can no longer be assumed, and thus the formation of metastable phases and microstructures are possible.[2] These non-equilibrium effects make surface treatment processes attractive.

Surface treatments using high-energy beams generally overcome three major difficulties, which are encountered in interpreting the rapid solidification microstructures resulting from other techniques, such as melt spinning or atomization. First, the liquid pool that is created during this process is contained by its own solid and generally no nucleation is involved. The microstructural evolution, therefore, can be treated purely as a growth phenomenon.[3] Second, it is possible to measure local growth velocity directly and correlate it with the corresponding microstructure. This is an important aspect because of the fact that growth velocity of the solid–liquid interface is found to be the single most important variable controlling microstructural selection during the process of laser resolidification. Third, the intimate contact of the surface-melted layer with the substrate makes it easier to compare the results with numerical heat flow models.[4]

Because microstructural evolution is strongly influenced by the solidification velocity (V), it is imperative to determine V experimentally as precisely as possible. The following approach has been adopted to determine the local solidification velocity in the current work.[5] During the laser remelting process at a fixed laser power and constant scanning speed, a steady-state pool is created. Under constrained growth conditions, the velocity of the solidification front is determined by the thermal field. Because the velocity of the solidification front (V) is along the maximum temperature gradient (*i.e.,* along the direction normal to the solid–liquid interface), V can be obtained by the following equation:

$$\vec{V} = \vec{V_b} \cdot \vec{n} = \vec{V_b} \cdot \cos\theta \qquad [1]$$

where $\vec{n}$ is the unit vector normal to the solid–liquid interface, V_b is the laser beam scanning velocity, and θ is the local angle between V and V_b. In experiments, θ can be measured in two ways: either by measuring the orientation of the grain boundaries or by measuring that of the interdendritic phase with respect to the known laser scanning direction. Therefore, the possibility of relating the experimentally measured growth velocity with the microstructure opens up a way to understand microstructural evolution in the remelted layers.

Although research of rapid solidification of dilute alloys using different techniques is well-known, studies of nucleation and growth kinetics of concentrated alloy systems that contain ordered compounds are scarce in the literature and are not well understood.[6–10] Kurz *et al.*[1,6–12] have studied the phase selection process during laser resolidification of Al-rich Al-Cu and Al-Fe alloys. These authors have provided a map of composition and growth rate for microstructural selection in these binary systems. However, phase selection and development of the morphology of the advancing solid–liquid interface for concentrated alloy systems is a field that remains to be explored. The current work is an endeavor toward understanding phase selection and morphological evolution during the process of laser resolidification of a concentrated Fe-Ge alloy containing a 25-atom pct solute. This alloy composition (Figure 1) shows

KRISHANU BISWAS, Graduate Student, and KAMANIO CHATTOPADHYAY, Professor, are with the Department of Metallurgy, Indian Institute of Science, Bangalore, India. Contact e-mail: kris@met.iisc.ernet.in

This article is based on a presentation made in the symposium entitled "Solidification Modeling and Microstructure Formation: In Honor of Prof. John Hunt," which occurred March 13–15, 2006, during the TMS Spring Meeting in San Antonio, Texas, under the auspices of the TMS Materials Processing and Manufacturing Division, Solidification Committee.

the presence of a peritectic reaction involving ordered compounds.[13] The motivation of the current work derives from our investigation of the undercooling of this alloy using the electromagnetic levitation facility. It has been found[14,15,16] that this alloy (indicated by the black arrow on the phase diagram in Figure 1) undergoes a peritectic reaction involving the ordered α_2 (B2) phase and a liquid leading to the formation of the ordered ε (DO_{19}) phase. The peritectic reaction is suppressed in deeply undercooled samples, and ε has been found to form from the α_2 phase via solid-state transformation.[14–16] Attention can also be drawn to the eutectic reaction close to this peritectic reaction: $L \rightarrow \varepsilon + \beta$. The final microstructures of the undercooled samples show the presence of interdendritic eutectic between ε-β as observed by using a transition electron microscope (TEM).[14]

II. EXPERIMENTAL DETAILS

Fe-Ge alloys containing 25 atom pct Ge were prepared by arc melting high-purity Fe (99.9 pct purity) and Ge (99.999 pct purity). The samples were melted repeatedly to have compositional homogeneity. Chemical analysis was performed on selected specimens by electron probe microanalyzer (EPMA), and the measured compositions of alloys were 25 atom pct with a scatter of ± 0.3 atom pct. The surface on which laser treatment was to be done was polished flat. Prior to the laser treatment, all samples were ground on 100 grit SiC paper to ensure a similar surface quality of each specimen and to enhance the absorption of the laser beam. Rapid solidification experiments were carried out using a continuous-wave 10-kW CO_2 laser (ROFIN SINAR). To refine the inhomogeneous as-cast microstructure, all specimens underwent double laser treatments. In the first case, the sample surface was scanned by overlapping laser traces (parallel to the polishing direction) over the whole surface at a relatively moderate laser power density of 1.2×10^4 W/cm^2 and an interaction time of 1×10^{-2} second. These ensure compositional homogeneity over a large depth (200 to 300 μm). Several experiments were performed prior to the final resolidification experiment on this alloy. Initial trials were done using different power and scanning speeds to obtain a stable melt pool. Melting of single traces was carried out with 3-kW laser power and different scanning speeds (V_b). The details of the parameters used for laser treatment are summarized in Table I. During the laser treatment, a continuous flow of argon gas (8 L/minute) was maintained to prevent oxidation of the molten pool.

Microstructural analysis of the remelted layers was carried out using scanning electron microscope (SEM; JEOL JSM 840A, FEI SIRION) operating at 20 kV. The chemical analyses were performed using the CAMECA SX100 EPMA operating at 20 kV and 40 nA. The phase analysis was done using a TEM (JEOL 2000FXII) operating at 200 kV. The samples for the TEM were prepared using the standard cross-section method. In the next section, the microstructure of the as-cast specimen is presented first, followed by microstructural evolution of the remelted layers treated at three different laser scanning speeds: 5, 11.7, and 16.7 cm/second.

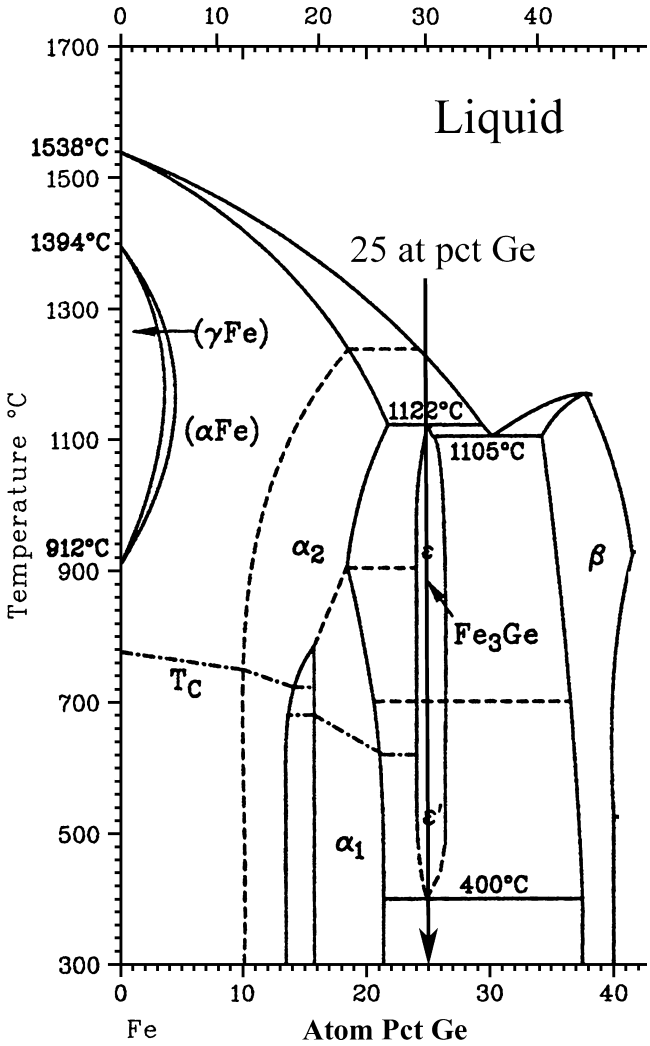

Fig. 1— Equilibrium phase diagram of Fe-Ge system.[13] The black arrow indicates the alloy composition under study.

Table I. Experimental Values of the Melt Pool Depth, Width as a Function of Power Intensity, and Traverse Speed (V_b) for Representative Samples for the Alloy Fe-25 Atom Pct Ge

Power Intensity (W/cm^2)	Interaction Time (second)	Traverse rate (cm/second)	Depth (μm)	Width (μm)
1.7×10^5	3×10^{-2}	5×10^{-2}	225	825
1.7×10^5	1.3×10^{-2}	11.7×10^{-2}	170	815
1.7×10^5	9×10^{-3}	16.7×10^{-2}	60	765

III. RESULTS

A. *As-Cast Microstructure*

Figure 2 shows the microstructures of the as-cast specimen. The optical micrograph as shown in Figure 2a reveals the presence of three phases. The primary phase, α_2 dendrite, is surrounded by the ε phase, which has formed as a result of a peritectic reaction between the α_2 phases and liquid. The ε phase is called the peritectic phase. The third growth morphology is the lamellar eutectic between ε and β. All the phases are marked on the figure. To reveal

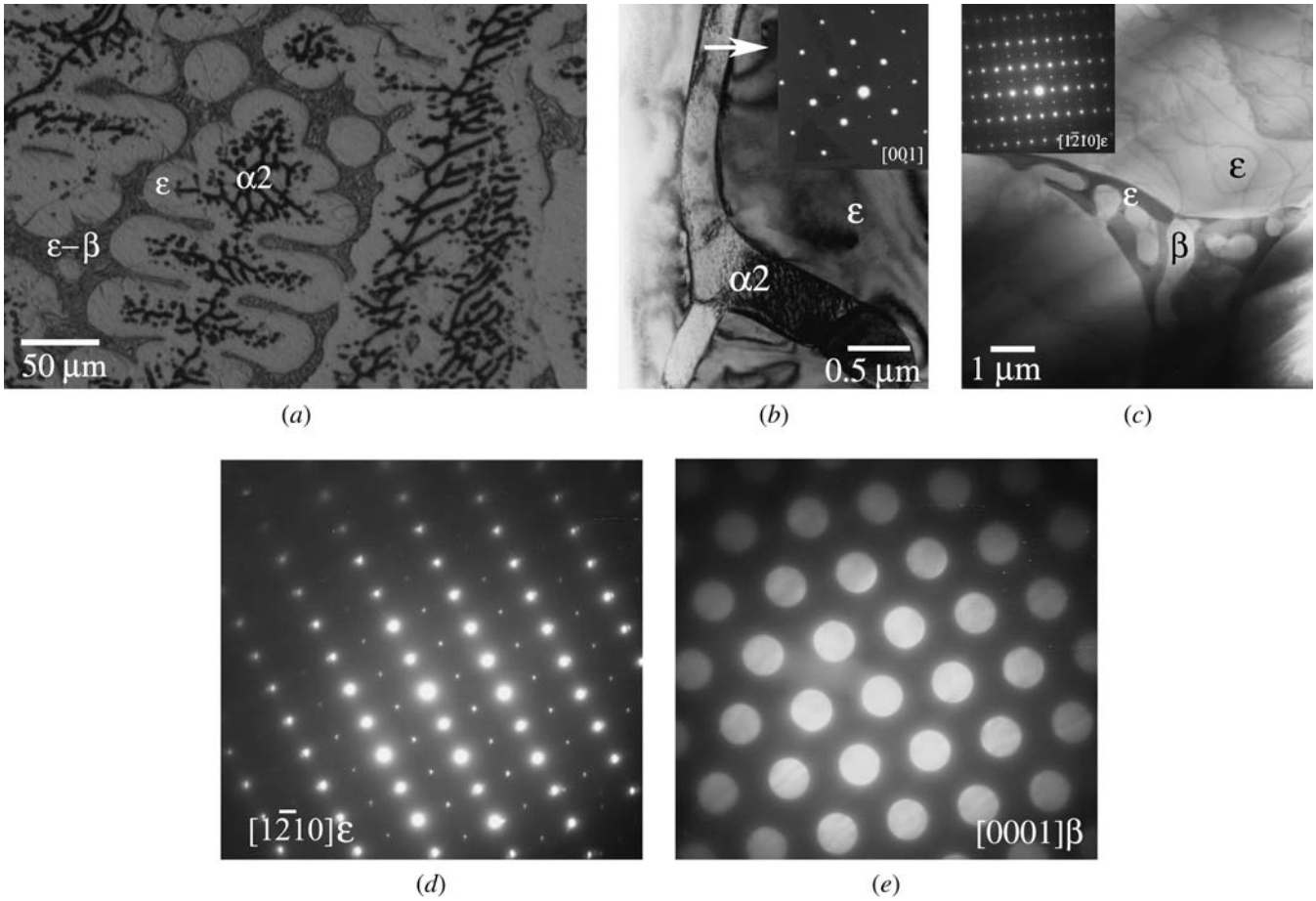

Fig. 2—As-cast microstructure. (*a*) Optical micrograph showing different phases and morphologies. (*b, c*) Bright-field transmission electron micrographs showing different phases, with inset showing selected area diffraction (SAD) patterns from the α_2 and ε phases respectively. (*d, e*) SAD pattern and microdiffraction pattern taken from ε and β lamellae of the eutectic respectively.

the structure of these phases, a detailed TEM study was carried out. The low-magnification bright field images show (Figure 2b and 2c) the presence of the α_2 and ε phases along with the ε-β eutectic. The insets in the figures show selected area diffraction (SAD) patterns as obtained from the α_2 and ε phase respectively. The presence of superlattice reflections confirms the ordered nature of the phases. Figure 2c shows the presence of the eutectic as marked on the figure. The SAD pattern and the microdiffraction pattern as shown in Figure 2d and 2e confirm that the eutectic lamellae are ε and β respectively.

B. *Composition Analysis of the Remelted Layers*

The EPMA analysis was utilized to obtain the composition of the remelted layers. Figure 3a through 3c shows the composition profiles of the remelted layers studied. The composition of the remelted layers fluctuates across the height of the layers. In case of the low-velocity remelted sample (5 cm/second), the remelted layer (Figure 3a) is found to be rich in Ge content compared with the starting alloy composition. The average composition of the remelted layer is 26.5 atom pct Ge. For the sample treated with a laser scanning speed of 11.7 cm/second (Figure 3b), the composition profile shows that the bottom of the remelted layer contains about 25.5 atom pct Ge, but later the composition increases to 27 atom pct Ge. The composition profile of the sample remelted with a laser scanning velocity of 16.7 cm/second (Figure 3c) yields nonuniformity across the whole remelted pool, fluctuating from 24 to 26.5 atom pct Ge (mean, 25 atom pct Ge).

C. *Microstructure Evolution in Remelted Layers*

1. *Sample resolidified at a laser scanning speed of 5 cm/second*

Microstructural evolution during laser resolidification using a scanning speed of 5 cm/second is shown in Figures 4 and 5. Figure 4(a) is the SEM micrograph of the longitudinal section of the remelted layer. The remelted layer is seen at the top of the figure. The depth of the resolidified layer is about 225 μm. The surface that demarcates the resolidified layer from the bulk is found to be very sharp. The higher magnification micrograph of the remelted pool (Figure 4(b)) reveals the growth of eutectic across the height of the remelted layer. The eutectic is lamellar in nature. The bottom of the remelted layer shows growth of eutectic colonies. At the top of the remelted layer, the eutectic lamellae are very fine (interlamellar spacing, which characterizes the length scale of the cooperative growth, is of the order of 100 nm). The inset of Figure 4(b) shows a representative high-magnification micrograph of the region

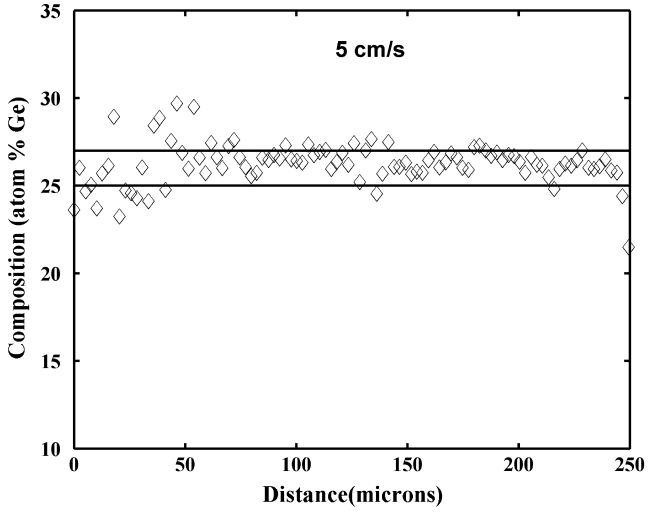

(*a*)

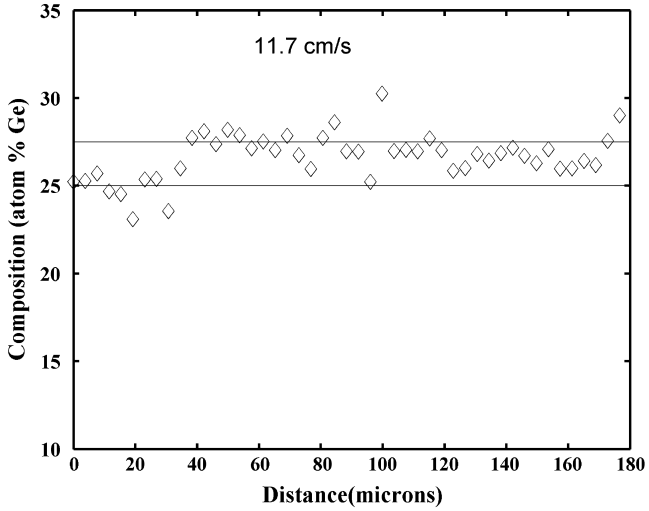

(*b*)

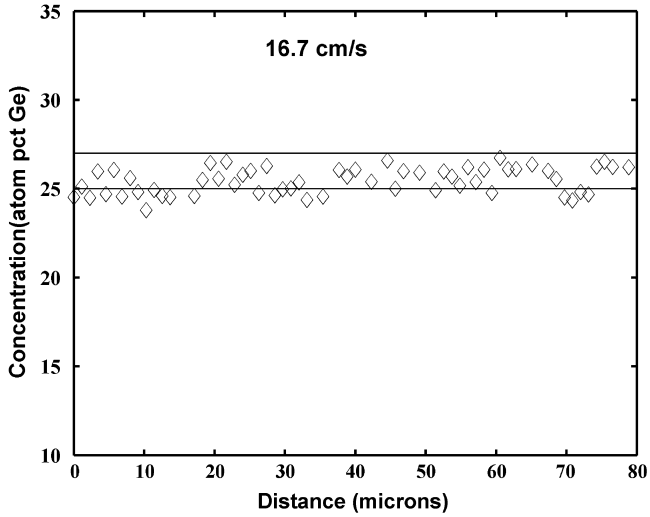

(*c*)

Fig. 3—(*a–c*)Composition profiles of laser trace from the bottom to the top of samples resolidified at a laser scanning speed of (*a*) 5 cm/second, (*b*) 11.7 cm/second, and (*c*) 16.7 cm/second.

near the top of the remelted layer showing lamellar fine-scale eutectic.

TEM observation of this sample is presented in Figure 5. The typical bright field micrograph (Figure 5(a)) shows the lamellar nature of eutectic in the remelted pool. The microdiffraction pattern taken from the wider lamella is shown in Figure 5(b). The microdiffraction patterns can be indexed using the lattice parameter of α_2 phase (a = 0.288 nm). A similar analysis for other lamellae is shown in Figure 5(c). The microdiffraction pattern indicates the phase to be β (a = 0.3998 nm and c = 0.501 nm). The dark field image (Figure 5(d)) taken using a β reflection ($\vec{g} = (11\bar{2}0)$) lights up all the β lamellae.

2. *Sample resolidified at a laser scanning speed of 11.7 cm/second*

This section presents the microstructural evolution when the same alloy is rapidly resolidified at a higher laser scanning speed of 11.7 cm/second. The low-magnification micrograph of the longitudinal section of the remelted layer (as shown in Figure 6(a)) shows the half of the remelted pool. The microstructural evolution from the bottom to the top of the remelted layer exhibits different growth morphologies. The bottom of the remelted layer shows the lamellar eutectic growth morphology, which undergoes a transition to a mixture of the dendrite and eutectic colonies as the interface moves toward the top of the layer.

To reveal the morphological transition at the bottom of the remelted layer, the higher magnification secondary electron image of the region near the bottom of the pool is shown in Figure 6(b). The change in the scale of microstructure at the bottom of the pool yields a sharp boundary between the base alloy and the remelted pool. The beam scanning direction is also indicated on the micrograph. This image shows that the growth of the remelted layer begins with lamellar eutectic morphology. Subsequently, this eutectic growth front breaks down into a dendrite growth front, with interdendritic liquid solidifying as eutectic. The SEM image of the top portion of the remelted layer (inset of Figure 6(b)) reveals the growth of the dendrite plus eutectic morphologies.

Figures 7 and 8 show the TEM observations of the remelted layer. We will concentrate mainly on the top portion of the remelted region consisting of dendrite and eutectic microstructure. The typical low-magnification bright field image is shown in Figure 7(a). The SAD patterns taken from the dendrite are shown in Figure 7(b) and 7(c). The patterns can be indexed using reflections corresponding to the α_2 phase. The superlattice spots in [001] and [011] zone axes patterns indicate B2 ordering. The low intensity of superlattice spots ({100} type) in the [011] zone axis pattern is the result of incomplete ordering because of the process of rapid solidification. The dark field images (not shown here) taken using these superlattice reflections do not show any antiphase domains. Similarly, TEM analysis of the lamellar eutectic is presented in Figure 8. The bright field and dark field image pair of the eutectic is shown in Figure 8(a) and 8(c). SAD patterns taken from both the lamellae, as shown in Figure 8(b) and 8(d), indicate that the phases are α_2 and β respectively.

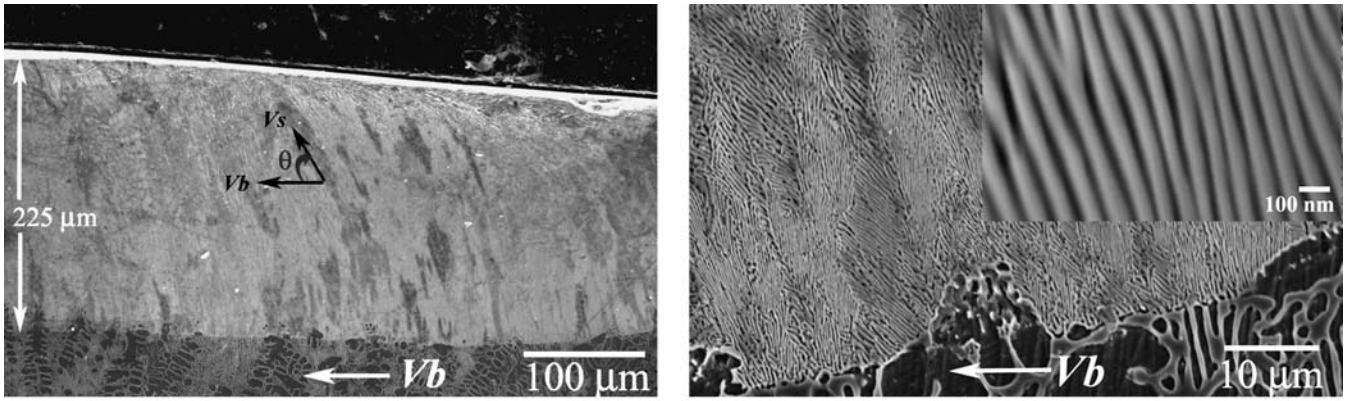

Fig. 4—Scanning electron microscope (SEM) micrographs of a sample resolidified at a laser scanning speed of 5 cm/second. (*a, b*) Low-magnification micrograph (*a*) of the longitudinal section and high-magnification micrograph (*b*) of the resolidified layer near the bottom of the trace. The inset in (*b*) shows an SEM micrograph of the top of the resolidified layer. The direction of the laser beam (V_b) and the solidification front (V) are indicated on the micrographs.

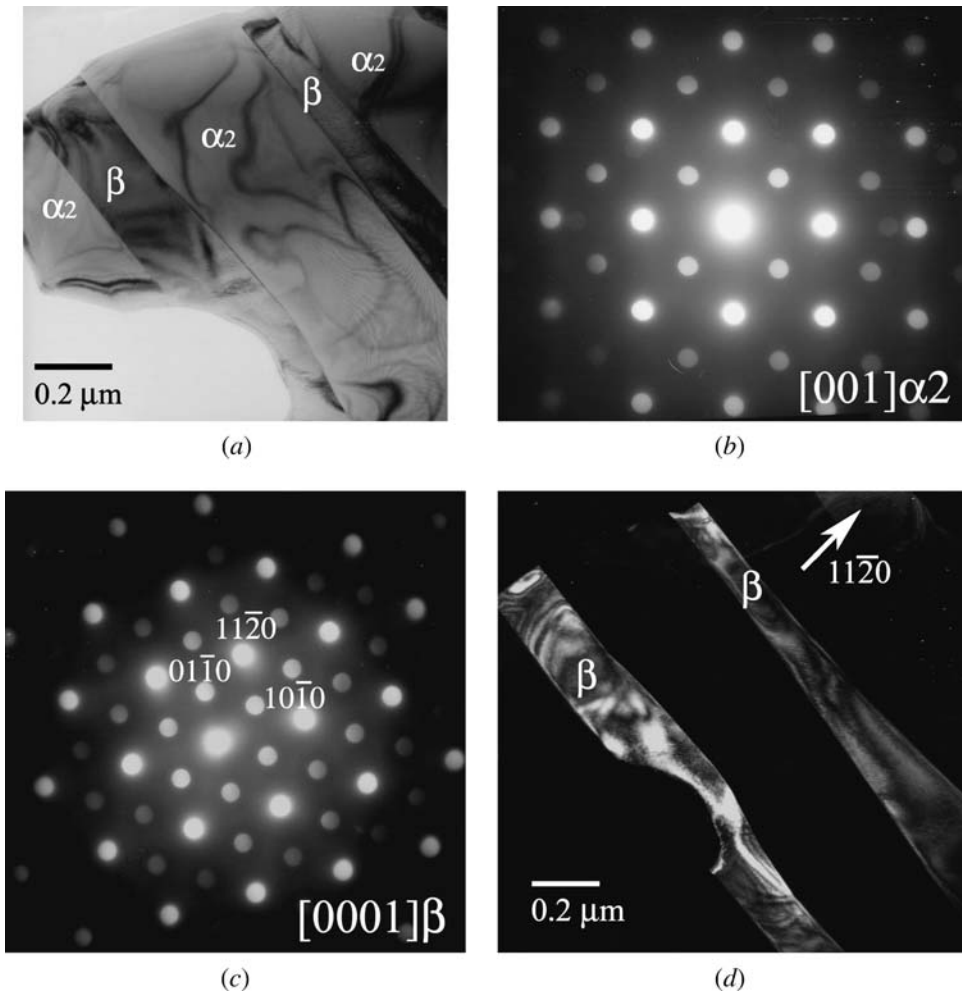

Fig. 5—(*a–d*) Bright field transition electron microscope micrograph of the lamellar eutectic (*a*), microdiffraction pattern taken from the lamellae confirming α_2 and β eutectic (*b, c*), dark field image using (11$\bar{2}$0) β reflection lighting up β lamellae (*d*).

3. *Sample resolidified at a laser scanning speed of 16.7 cm/second*

The microstructural evolution of Fe-25 atom pct Ge resolidified at a scanning rate of 16.7 cm/second is different from the previous two samples. The microstructure of the remelted layer is illustrated in Figure 9(a), which is a low-magnification secondary electron image of the longitudinal section of the remelted layer. The sharp transition from the

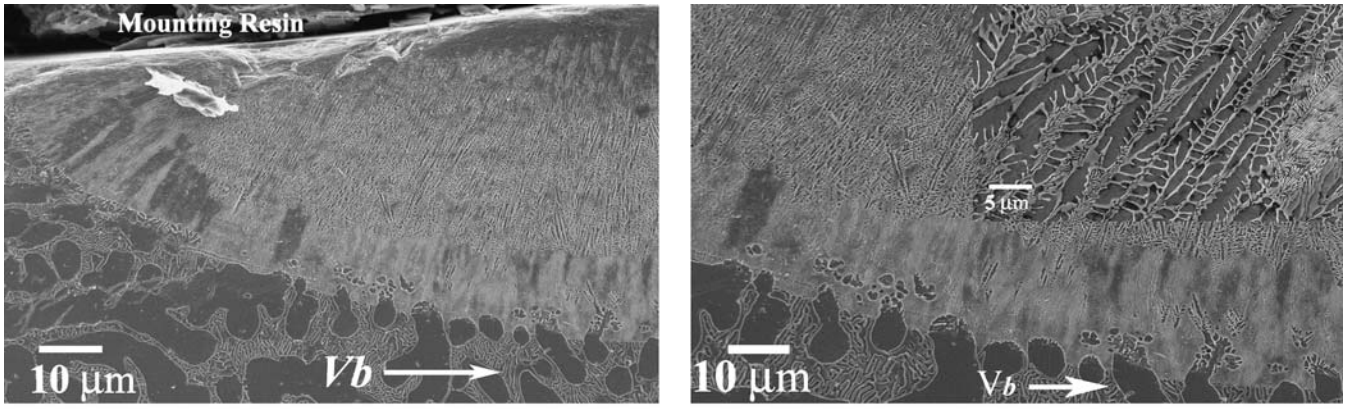

Fig. 6—Scanning electron microscope micrographs of a sample resolidified at a laser scanning speed of 11.7 cm/second. (*a, b*) Low-magnification micrograph of the longitudinal section (*a*) and high-magnification micrograph showing a morphological transition from the lamellar eutectic to dendrite, with interdendritic liquid solidifying as eutectic (*b*). The inset shows the higher magnification micrograph of the top portion of the resolidified layer revealing dendritic and eutectic morphologies.

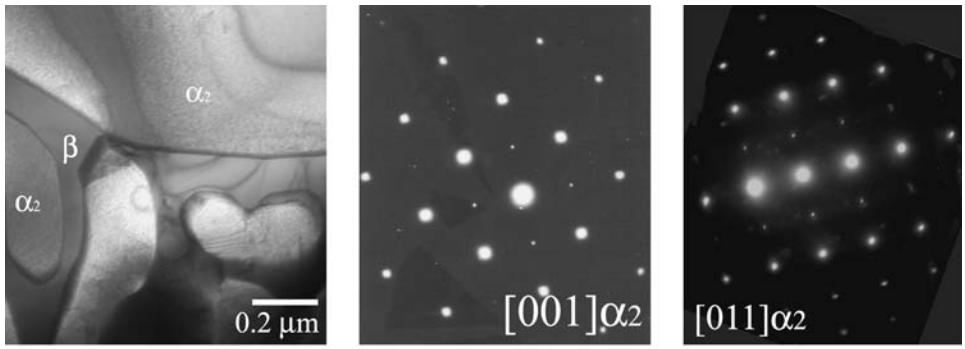

Fig. 7—Transition electron microscopie observation of the top portion of the resolidified sample processed with a laser scanning speed of 11.7 cm/second. (*a*) Bright field micrograph showing dendritic and eutectic growth morphologies. (b) Selected area diffraction patterns taken from the dendrite showing the dendrites are α_2.

coarse to the finer microstructural length scale depicts the sharp boundary between the laser-treated surface layer and the base material. Careful observation of the remelted pool shows two separate growth morphologies. At the lower part of the pool, one can observe the growth of the lamellar eutectic, which is later replaced with dendrite growth morphology.

The details of this morphological transition can be clearly observed in the higher magnification micrograph, as shown in Figure 9(b), with inset showing the low-magnification SEM micrograph, which indicates the place from where the image has been obtained. The eutectic growth front can grow only up to about 10 μm from the bottom of the pool. Subsequently, as the growth velocity of the solid–liquid interface increases, the dendrite growth front wins over the eutectic front. There is a sharp transition from the eutectic growth morphology to the dendrite growth morphology. This transition takes place at a well-defined position at the remelted layer, which corresponds to a well-defined growth velocity of the solid–liquid interface (discussed later). The higher magnification back-scattered image of the top portion of the remelted layer is shown in Figure 9(c). The dendritic growth morphology can be observed. The inset in Figure 9(c) is the low-magnification SEM micrograph showing the position from where the Back Scattered Electron (BSE) image has been obtained. The BSE image reveals the presence of another phase within the dendrites. Some of these phases are marked by white arrows.

The results of TEM observation of the sample are shown in Figure 10. A typical bright field image of the bottom of the remelted layer (Figure 10(a)) reveals growth of the lamellar eutectic. The eutectic lamellae grow along the direction of heat flow and thus bend depending on the change in the heat flow direction in the remelted layer. The microdiffraction patterns as observed from both the lamellae are shown in Figure 10(b) and (c) respectively. Analysis of these patterns indicates that the eutectic lamellae that grow from the bottom of the remelted layer are α_2 and β. Figure 10(d) shows a typical low-magnification bright field image of the top region of the remelted layer. The micrograph shows the presence of α_2 dendrites (SAD pattern as shown in the inset in Figure 10(d)) with an interdendritic region as β. The presence of another phase can be observed on the micrograph (marked by white arrows on the figure). Figure 10(e) shows a higher magnification image (Figure 10(e)) revealing the presence of this phase. This is similar to the microstructure shown in Figure 9(c). The microdiffraction pattern (Figure 10(f)) obtained from

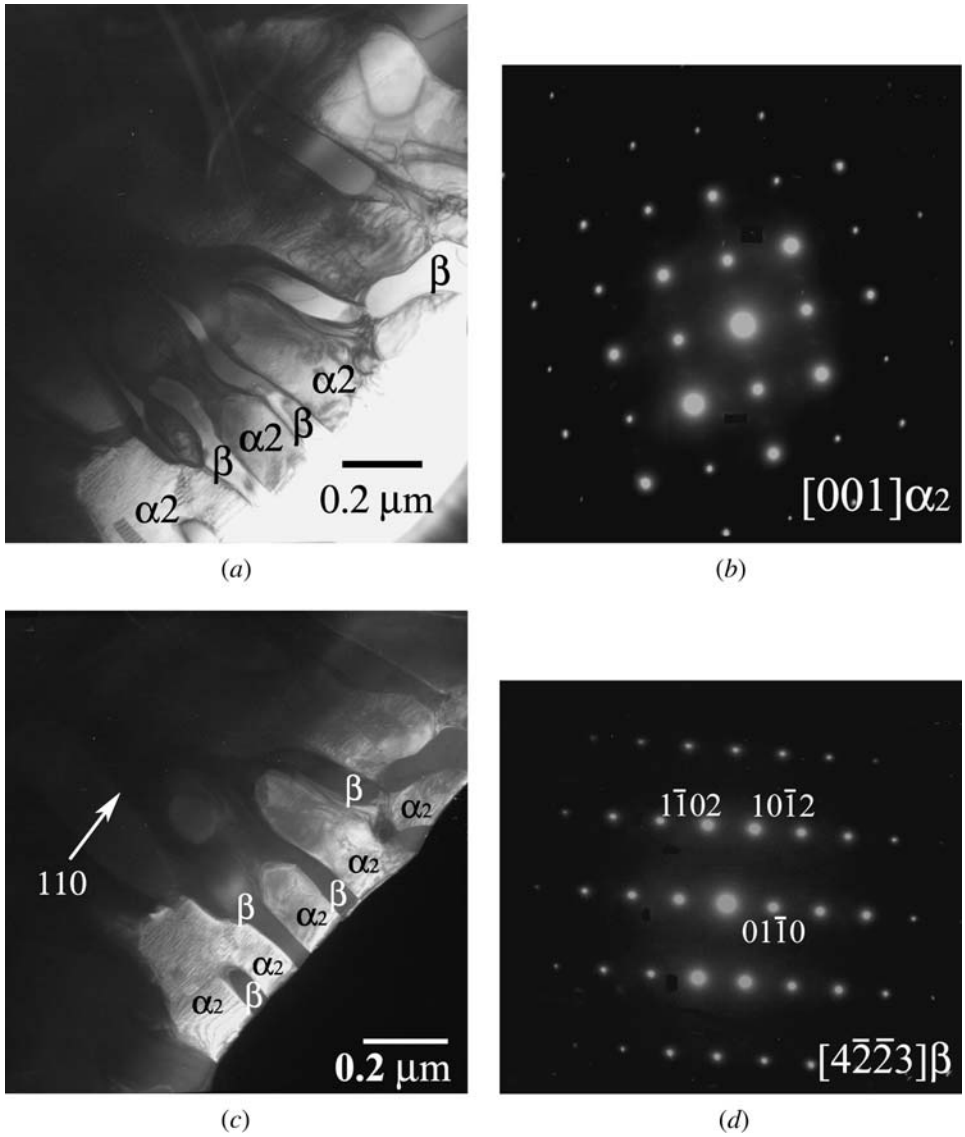

Fig. 8—(*a, c*) Bright field and dark field pair of the eutectic respectively. (*b, d*) Selected area diffraction patterns indicating an α_2-β eutectic.

this phase can be indexed in terms of ε phase (a = 0.5169 nm and c = 0.4222 nm).

D. *Growth Velocity Measurements*

The local growth velocity of the solid–liquid front (V) along the height of the laser trace of each sample was measured. According to the relationship presented in Eq. 1, one needs to measure the local angle, θ, between the microstructural features (eutectic lamellae or interdendritic phases) with a known scanning direction of the laser beam (V_b). Figure 4(a) shows the way the angle was measured to obtain local growth velocity. Using the secondary electron images obtained from longitudinal sections of all three samples, the measurements were carried out. A sufficient number of measurements (at least five at each point) were made so that measurement error is minimized. The average values of such measurements are reported here. Figure 11 shows the velocity of the solid–liquid interface as a function of distance from the bottom of the remelted layer for different beam scanning rates. Several important features can be observed from this figure. Microstructural development in the remelted layer started with the α_2-β eutectic growth front for three different laser scanning speeds. In the case of the lowest scanning rate (5 cm/second), the remelted layer shows growth of the α_2-β lamellar eutectic throughout the remelted layer, whereas higher scanning speeds lead to a morphological transition from the eutectic front to the dendrite. Therefore, the eutectic can grow up to a certain critical growth velocity of the solid–liquid interface (Figure 11) and was found to be about 3.4 cm/second. As the velocity of the growing interface increases above 3.4 cm/second, the eutectic growth front is not stable and the dendritic growth front wins over the eutectic front.

IV. DISCUSSION

In this section, several aspects of microstructural evolution relevant to the current investigation are discussed. The

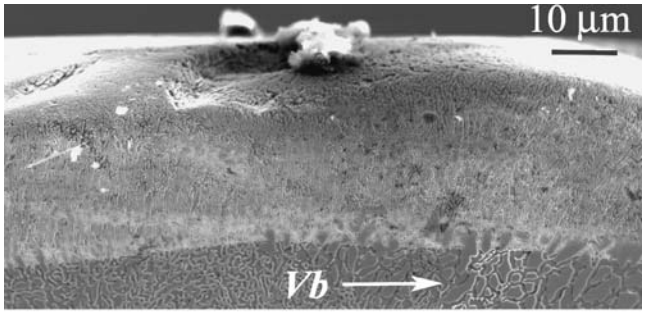

(*a*)

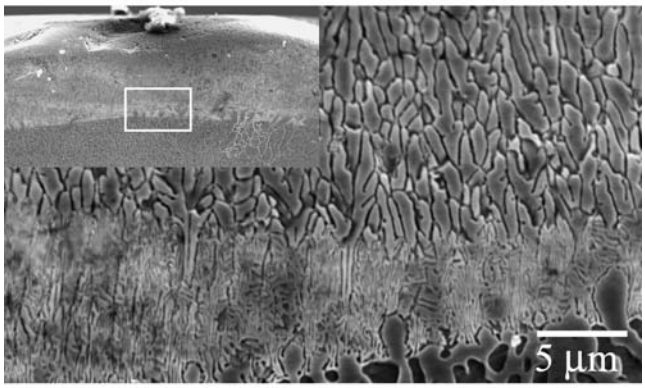

(*b*)

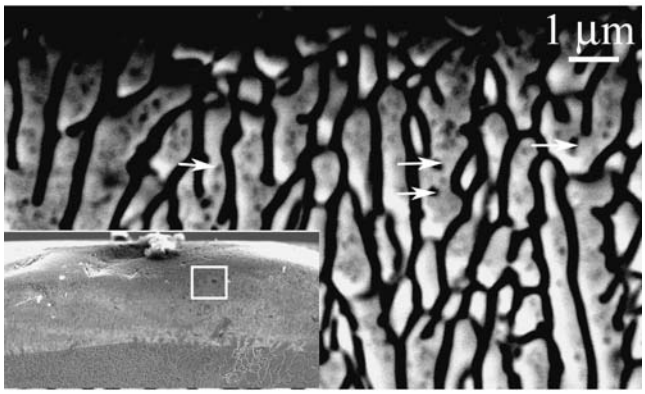

(*c*)

Fig. 9—Scanning electron micrographs of the sample resolidified at a laser scanning speed of 16.7 cm/second. (*a*) Low-magnification micrograph of the longitudinal section. (*b*) High-magnification micrograph of the bottom of the resolidified layer showing a morphological transition from eutectic to dendritic growth. (*c*) BSE image of the top portion of the resolidified layer showing the presence of a phase within the dendrites. The insets in *b* and *c* show the regions in the low-magnification micrographs from which the images were acquired.

formation of a metastable eutectic between α_2-β bypassing the peritectic reaction $\alpha_2 + L \rightarrow \varepsilon$ is explained first, followed by a discussion of various morphological transitions.

A close look at the phase diagram[13] near the alloy composition will shed some light on the mechanism responsible for the formation of the metastable eutectic. Such a construction is shown in Figure 12(a). The liquidus and solidus of α_2 and β are extended to construct an α_2-β eutectic phase field. The phase boundaries of the ε phase have been removed for the sake of clarity. The eutectic temperature of the metastable eutectic is slightly lower (~6K) than that of equilibrium eutectic between ε and β. The new eutectic composition is 30.1 atom pct Ge, which is 0.3 atom pct leaner in solute content than the equilibrium ε-β eutectic (C_e = 30.4 atom pct Ge). Therefore, the observed appearance of a eutectic between α_2 and β can be explained by postulating the existence of a metastable α_2-β eutectic ~6K below the stable ε-β eutectic.

To explain the observed microstructural transitions during the process of laser resolidification, we attempt to model microstructural evolution using a combination of plane front, dendritic, as well as eutectic growth models, taking into consideration the conditions of rapid solidification with consistent materials and thermophysical parameters. However, application of these growth theories requires steady-state conditions to be satisfied during the process of laser resolidification. The rapid movement of the solid–liquid interface during this process, from zero at the bottom of the trace to a maximum value at the surface, makes the application of the steady-state growth theories inappropriate for modeling the growth kinetics. According to Karma,[11] the equation that gives the establishment of a quasi steady-state condition in such a process is given by

$$\frac{\frac{D}{V}\cdot\frac{\partial V}{\partial x}}{V} \ll 1 \qquad [2]$$

Therefore, the quasi steady-state condition is satisfied if the change in V, when the interface moves a distance of (D/V), is much less than V. In the current case, such a condition is satisfied over the entire laser trace at all relevant growth conditions. Typical maximum value of $\Delta V/\Delta x$ is of the order of 10^4 to 10^5 per second, which gives a value of 10^{-4} to 10^{-3} for the left side of Eq. [2]. Therefore, steady-state growth theories can be applied to explain microstructural evolution during the process of laser resolidification.

Dendritic growth has been modeled using the Kurz–Giovenella–Trivedi (KGT) model.[17] This model is based on the Ivantsov solution of a parabolic needle crystal.[18] According to this model, the radius of a dendrite tip (R) is given by the smallest root of the quadratic equation

$$\frac{M}{R^2} + \frac{N}{R} + G = 0 \qquad [3]$$

where

$$M = 4 \cdot \pi^2 \cdot \Gamma$$

$$N = \frac{2 \cdot m \cdot C_0 \cdot P(1-k)\xi_C}{1-(1-k)\cdot Iv(P)}$$

G is the thermal gradient, Γ is the Gibbs–Thomson coefficient (ratio of surface energy to volumetric entropy of fusion), C_0 is the alloy composition, m is the velocity-dependent slope of the liquidus, k is the velocity-dependent partition coefficient, ξ_C is a function of the Péclet number ($P = VR/2D$), $Iv(P)$ is the Ivantsov function, and D is the solute diffusivity in liquid.

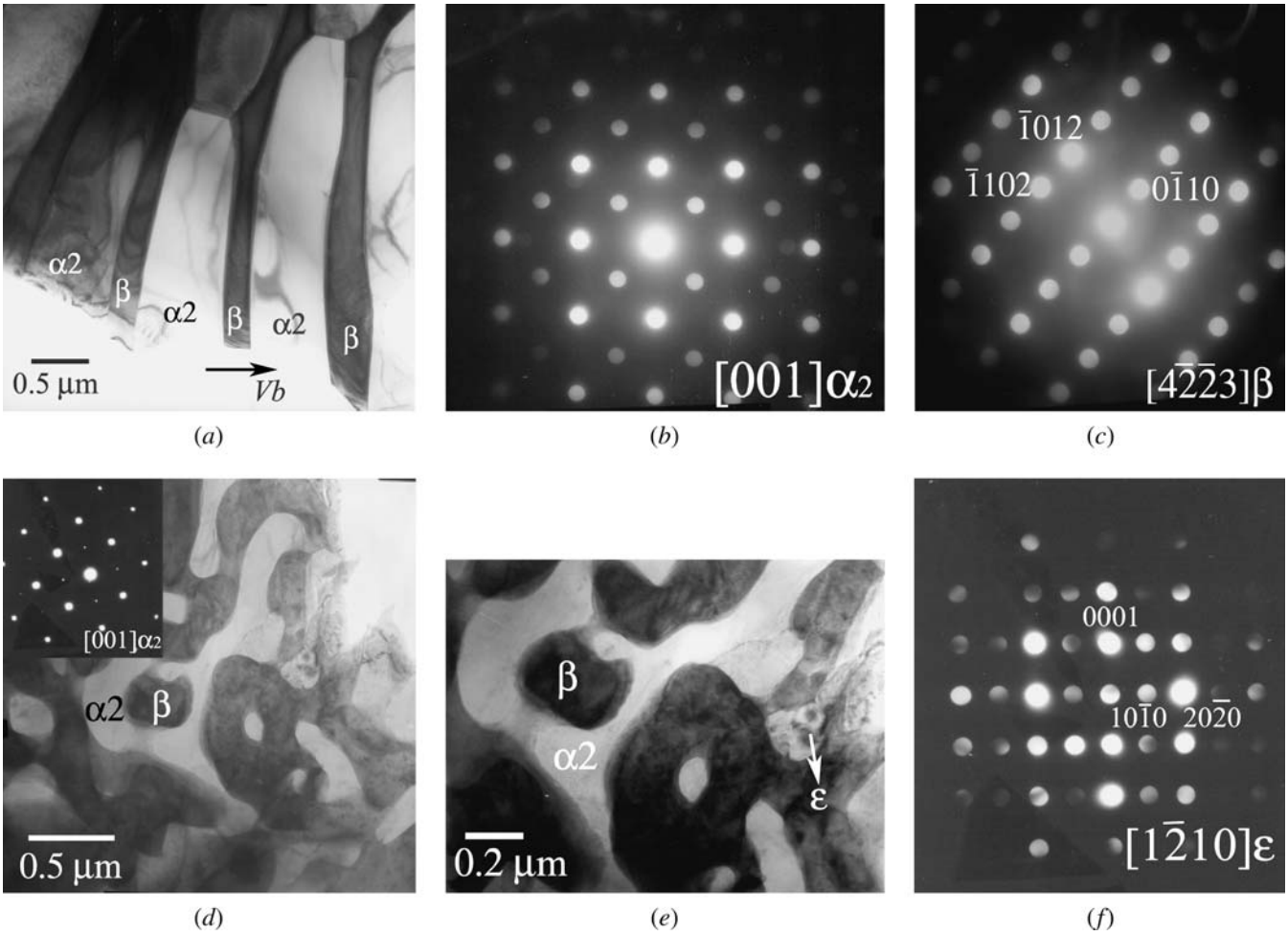

Fig. 10—Transition electron microscope observation of a resolidified layer processed with a laser scanning speed of 16.7 cm/second. (*a*) Bright field image of the lamellar eutectic observed at the bottom of the remelted layer. (*b, c*) Microdiffraction obtained from the lamellae indicating an α_2-β eutectic. (*d*) Low-magnification bright field image of the top portion of the resolidified layer. (*e*) Higher magnification bright field image showing the presence of a phase within the α_2 dendrites. (*f*) Microdiffraction showing that the phase precipitated is ε. The inset in *d* shows a [001] zone axis pattern of α_2 dendrites.

$$\xi_C = 1 - \frac{2k}{\{1 + [(2\pi/P)^2]^{1/2} - 1 + 2k\}}$$

Solute trapping has been modeled using velocity dependence of the partition coefficient:[19]

$$k(V,T) = (k_e(T) + V/V_D)/(1 + V/V_D)$$

where $k_e(T)$ is a function of temperature because of nonlinearity of solidus and liquidus curves.

It is assumed here that the solute trapping model by Aziz[19] gives the appropriate behavior for high-solute concentrations as well. The dependence of the partition coefficient on temperature, velocity, and concentration given by Aziz and Kaplan[20] was not used because the thermodynamic data of all relevant solid phases of the Fe-Ge system are not available in the literature.[21] The application of the expression given by Aziz and Kaplan[20] requires the calculation of driving free energy for liquid–solid transformations, which requires heat capacity data of all relevant phases. To the best of our knowledge, such a data are only available for the α_2 phase at different Ge concentrations.[22]

The Nonequilibrium liquidus slope[23] as given by following expression was utilized.

$$m(V,T) = m_0\left(1 - \frac{1 + (k_e - k(1 - \log(k/k_e))/1 - k_e}{1 - (1 - k)Iv(P)}\right)$$

where k_e is the equilibrium partition coefficient, which is a function of temperature. V_D is known as the interface diffusive velocity.[19] The thermal gradient, G, was calculated according to the heat transfer model,[4,24] and an average value of 5×10^4 K/m was used for numerical calculations. Using thermophysical parameters (as given in Table II[25]), Eq. [3] is solved numerically to obtain a unique solution of *R* as function of *V*. The dendrite tip temperature is given by

$$T_d = g(C_l^*) - \frac{2\Gamma}{R} - (R_g T_l^2/\Delta H_f)\left(\frac{V}{V_0}\right) \qquad [4]$$

where C_l^* is the composition of the liquid at the dendrite tip,

$$C_l^* = \frac{C_0}{1 - (1 - k)Iv(P)} \qquad [5]$$

which is obtained from numerical solution of the KGT equation,[17] $g(C_l^*)$ is the temperature of the equilibrium liquidus at a solute concentration of C_l^*, and $2\Gamma/R$ is the curvature undercooling. The third term on the right side of Eq. [4] is the kinetic undercooling. V_0 is the kinetic parameter. For ordered phases, such as α_2 and ε, $V = V_d$ is used, and for the β phase, $V = V_s$ is utilized. V_s is the velocity of sound in the melt. R_g is the universal gas constant.

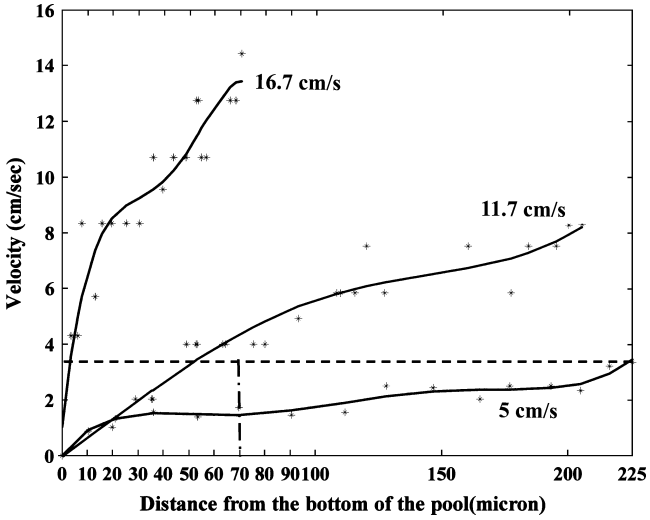

Fig. 11—Experimentally measured local growth velocity as a function of distance from the samples resolidified at different laser speeds. The solid lines indicate fitted lines.

Eutectic growth is modeled using the Trivedi–Magnin–Kurz (TMK) model.[26] This model is essentially an extension of the Jackson–Hunt model[27] with the growth rate at the extremum. However, the TMK model takes into account the conditions pertaining to rapid solidification with a high Péclet number ($Pe = V_s\lambda/2D$, where D is solute diffusivity and λ is the interlammellar spacing). Solution to the eutectic growth problem is available under two conditions that allow simplifications to be made on the generalized equation:[26,28] (a) a ''cigar-shaped'' liquidus and solidus of the phase diagram where the partition coefficient, k, of two phases varies from its value at a eutectic temperature to unity as the undercooling increases and (b) $k\alpha_2 = k_\beta$ (k_ε) = constant. In the current case, neither solution is correct. Nonetheless, case b is used here with a average value of $k(T) = \{k_{\alpha 2}(T) + k_\beta(T)/2$ or $k(T) = \{k_\varepsilon(T) + k_\beta(T)/2$, where T is the interfacial temperature. Comparison with predictions made using a cigar model shows little variation in qualitative behavior. The effect of solute trapping was included by using growth rate dependence of the partition coefficient according to Aziz.[19] The temperature dependence

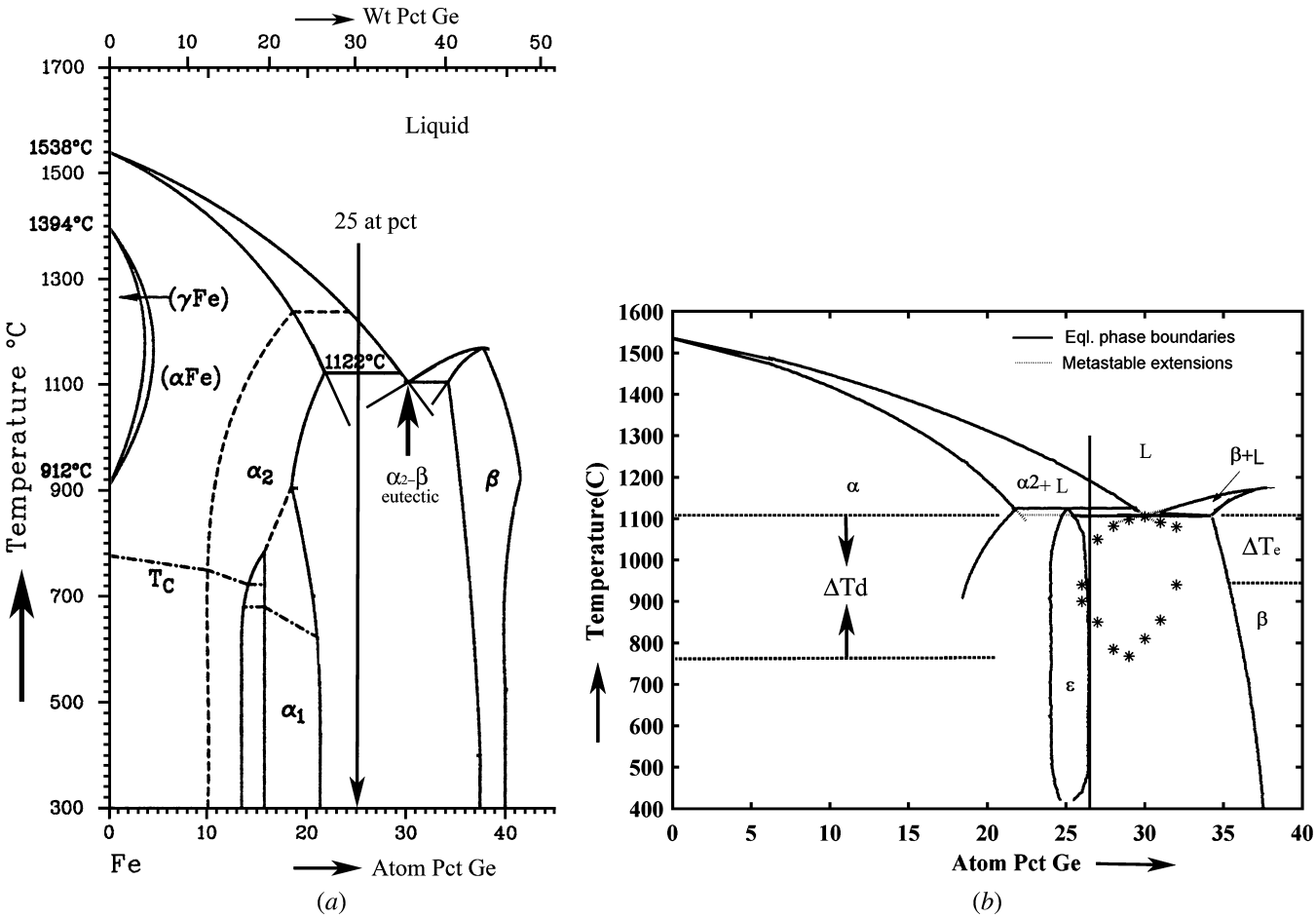

Fig. 12—(*a*) Postulated phase diagram construction for the existence of a metastable eutectic α_2-β (*b*) Calculated coupled zone of metastable eutectic α_2-β to explain the observed morphological transitions.

Table II. Thermophysical Parameters Used for Modeling of Solidification

Parameters	Values	Reference
Preexponential constant for diffusion, D_0 (m^2/second)	4.8×10^{-7}	[25]
Activation energy for diffusion, Q (kJ/mol)	58	[25]
Gibbs–Thomson coefficient of α_2, $\Gamma_{\alpha 2}$ (K.m)	2.93×10^{-7}	[14]
Gibbs–Thomson coefficient of β, Γ_β (K.m)	1.0×10^{-7}	[14]
Gibbs–Thomson coefficient of ε, Γ_ε (K.m)	3.1×10^{-7}	[14]
Interface diffusive speed, V_d (m/second)	5	[14]
Speed of sound, V_s (m/second)	2000	
Mean temperature gradient, G (K/cm, using heat flow calculations)	5×10^4	[4]
Melting point of Fe (K)	1872	
Atomic attachment coefficient of α_2, $\mu_{\alpha 2}$ (m/second.K)	4.94×10^{-3}	[14]
Atomic attachment coefficient of β, μ_β (m/second.K)	2.58	[14]
Atomic attachment coefficient of ε, μ_ε (m/second.K)	3.34×10^{-3}	[14]
$k_{\alpha 2}(T) = 3.997 - 6.8354 \times 10^{-3}T + 4.69395 \times 10^{-6}T^2 - 1.014 \times 10^{-9}T^3$		
$k_\beta(T) = 3.7 - 1.91 \times 10^{-3}T + 5.61 \times 10^{-6}T^2$		
$k_\varepsilon(T) = 11.34$		
$g_{\alpha 2}(C) = 1833.2 - 16.69 * C + 0.60641 * C^2 - 3.5186 \times 10^{-2} * C^3$ ($g_{\alpha 2}$(C) in °K)		
$g_\beta(C) = 3200 - 2.0 \times 10^2 C + 6.9 * C^2 - 7.5 \times 10^{-2} * C^3$ (g_β(C) in °K)		
$g_\varepsilon(C) = 1406.8 - 5 \times 10^{-1} * C + 1.0 \times 10^{-2} * C^2$ (g_ε (C) in °K)		

of diffusivity, *D,* is taken into account by using an Arrhenius-type expression. Because of a lack of experimental data, no attempt was made to take in to consideration composition dependence of diffusivity.

The interface temperature of plane front growth is given by the temperature of the solidus of the α_2, ε, and β phases at a particular alloy composition. However, solute trapping was incorporated into the model, and thus the position of the solidus becomes growth velocity dependent. Temperature-dependent diffusivity was also taken into account, as discussed in the case of eutectic growth. Kinetic undercooling was included using the following relationship:[29]

$$\Delta T_K = \frac{R_g \cdot T_m^2}{L} \cdot \frac{V_s}{V_0} \qquad [6]$$

where R_g is the universal gas constant, T_m is the melting point of the pure element, and L is the latent heat of fusion. Although T_m and L are known with varying degrees of certainty, it is difficult to obtain a value for V_0. For the α_2 and ε phases, $V_0 = V_d$, whereas for the β phase, $V_0 = V_s$ is used, where V_s is velocity of sound in the melt.

Using the approach described here, relevant interface temperatures of all phases and morphologies can be determined. Different microstructural transitions can be predicted by selecting the condition of the highest interface temperature. This is known as the competitive growth criterion.

In the current case, the interface temperature of the α_2, β, and ε dendrites; the ε-β and α_2-β eutectics; and the α_2 and β plane fronts at different composition of the melt were calculated. The morphological transition from the eutectic growth morphology to the dendritic plus eutectic to dendritic growth morphologies is a typical problem of competitive growth of different phases and morphologies. This can be explained using the concept of the coupled zone of the metastable eutectic between α_2-β. The coupled zone is defined as the range of conditions (composition and undercooling values) that produces a fully eutectic microstructure (*i.e.,* without primary crystals). It was previously shown that the relative interface temperatures at a given growth velocity or relative growth rates at a given level of undercooling will determine what phase and morphology will prevail under nonequilibrium conditions. The relative interface temperatures at a given growth rate from composition from 24 to 33 atom pct Ge of the alloy were calculated for all possible growth morphologies. Using these interface temperatures at a given composition of the alloy, we constructed the coupled zone† between α_2 and β. Such a coupled zone is shown in Figure 12(b). The dotted lines are extension of the liquidus and solidus lines of α_2 and β. The compositional measurements using EPMA show that the remelted layer is enriched with solute with an average composition of 26.5 atom pct, instead of 25 atom pct Ge of the base material. The black solid line in the figure indicates the composition of the remelted zone. Microstructural evolution in the remelted layers clearly suggests that the peritectic reaction (α_2 + *Liquid* → ε at 1122 °C [or 1395 K]) is bypassed and the liquid gets undercooled substantially by a minimum amount (ΔT_e = 125 °K) and enters into the coupled zone of the metastable eutectic between α_2 and β. Therefore, the microstructure in the remelted layer of the sample remelted at 5 cm/second shows the growth of the α_2-β eutectic from the bottom of the layer. This eutectic can grow easily inside the coupled zone because the coupled zone represents the range of growth conditions within which the morphologically stable two-phase growth can be obtained. As the scan rate of the laser increases, the liquid gets more and more undercooled. When the sample is processed with a laser scanning rate of 16.7 cm/second, the liquid can get deeply undercooled (by a minimum amount of $\Delta T_d \sim 325$ K) such that growth conditions favor the growth of dendrite morphology instead of eutectic.

†Efforts are made to apply the expression of partition co-efficient by Aziz and Kaplan[19] and composition as well as undercooling values corresponding to the upper part of the coupled zone has been determined using thermodynamic data of α_2 phase. The difference in composition and undercooling values is about 2.5 pct and 1 pct from the values reported here.

The experimentally measured growth velocity (Figure 11) of the solidification front suggests that there is a maximum velocity beyond which cooperative growth is no longer possible, and the eutectic growth front can be taken over by the dendritic growth. This velocity (V_{end}) has been found to be 3.4 cm/second. In the original TMK model, V_{end} can be obtained explicitly. For $V > V_{end,}$ the magnitude of the characteristic diffusion length scale is the same or less than the approximate diffusion distance for cooperative growth: $\lambda/2$. Therefore, solute redistribution by coupled growth is no longer possible for higher values of V, and dendrite growth morphology is the preferred one. However, in the current calculation, the partition coefficient, k, is temperature dependent, and the iterative process used to solve the equation stops converging at high Péclet ($Pe = V\lambda/2D$) numbers. In such as situation, V_{end} is taken as the velocity at which the solution failed to converge. The value of V_{end} as obtained from numerical calculation is found to be 3.1 cm/second for an average composition of 26.5 atom pct Ge, which is lower than the experimentally observed value.

Another important characteristic of rapidly solidified microstructures is the formation of an ordered ε phase in the sample processed by a laser scanning speed of 16.7 cm/second. Detailed SEM and TEM (Figures 9 and 10) observations reveal the presence of an ε phase within the α_2 dendrites. This phase was not observed in the samples processed with lower laser scanning velocities. Our results suggest that α_2 dendrites grow fast enough during laser processing at a scanning speed of 16.7 cm/second to form a supersaturated α_2 phase. The ε phase can then precipitate from the supersaturated α_2 dendrites in the solid state. Although direct evidence is difficult to obtain in the current case, the following argument points toward this possibility.[13,14] The compositional analysis of the α_2 dendrites ($\sim$24.5 atom pct Ge) shows that the α_2 phase solidifies nearly with the same composition as that of the ε phase ($\sim$25 atom pct Ge) as a result of solute trapping. The morphology of the ε phase (within the α_2 dendrites) also supports the argument.

V. CONCLUSIONS

1. Microstructural evolution of an Fe-25 atom pct Ge alloy during controlled laser remelting and solidification experiments was complex. There are several morphological transitions as the velocity of the solid–liquid interface increases.
2. The peritectic reaction involving α_2 and liquid leading to formation of ε is bypassed, and the liquid gets deeply undercooled to produce a metastable eutectic between α_2 and β.
3. Morphological transition from eutectic to dendrite plus eutectic to fully eutectic can be explained using the concept of competitive growth. Calculation of the coupled zone supports this scenario.

ACKNOWLEDGMENT

Authors thank Dr.Rolf Galun, University of Clausthal, Claustal-Zellerfeld, Germany, for help in laser processing of alloys.

REFERENCES

1. M. Gremaud, M. Carrard, and W. Kurz: *Acta Metall. Mater.*, 1991, vol. 39, pp. 1431-43.
2. G. Sepold and R. Becker: in *Science and Technology of Undercooled Melts*, R. Sahm, H. Jones, and C.M. Adams, eds., NATO ASI series, Martinus Nijhoff, Dordrecht, Germany, 1985, p. 112.
3. S. Yang, W.D. Huang, X. Lin, Y.P. Su, and Y.H. Zhou: *Scripta Mater.*, 2000, vol. 42, pp. 543-48.
4. G. Phanikumar, P. Dutta, R. Galun, and K. Chattopadhyay: *Mater. Sci. Eng. A*, 2004, vol. A371, pp. 91-102.
5. M. Rappaz: *Int. Metal Rev.*, 1989, vol. 34, pp. 93-123.
6. M. Zimmermann, M. Carrard, and W. Kurz: *Acta Metall. Mater*, 1989, vol. 37, pp. 3305-13.
7. S.C. Gill, M. Zimmermann, and W. Kurz: *Acta Metall. Mater.*, 1992, vol. 40, pp. 2895-906.
8. S.C. Gill and W. Kurz: *Acta Metall. Mater.*, 1993, vol. 41, pp. 3563-73.
9. S.C. Gill and W. Kurz: *Acta Metall. Mater.*, 1995, vol. 43, pp. 139-51.
10. M. Gremaud, M. Carrard, M. Zimmermann, and W. Kurz: *Acta Metall. Mater*, 1992, vol. 40, pp. 983-96.
11. M. Gremaud, M. Carrard, and W. Kurz: *Acta Metall. Mater.*, 1990, vol. 38, pp. 2587-99.
12. P. Gilgien, A. Zryd, and W. Kurz: *Acta Metall. Mater*, 1995, vol. 43, pp. 3477-87.
13. T.B. Massalski: *Binary Alloy Phase Diagrams,* 2nd ed., ASM, OH, 1990, p. 1704.
14. G. Phanikumar, K. Biswas, O. Funke, D. Holland–Moritz, D.M. Herlach, and K. Chattopadhyay: *Acta Mater.*, 2005, vol. 53, pp. 3591-600.
15. K. Biswas, P.K. Das, and K. Chattopadhyay: *J. Mater. Res.*, 2006, vol. 21, pp. 174-84.
16. K. Biswas, G. Phanikumar, D.M. Herlach, and K. Chattopadhyay: *Mater. Sci. Eng. A*, 2006, in press.
17. W. Kurz, B. Giovanella, and R. Trivedi: *Acta Metall. Mater.*, 1986, vol. 34, pp. 823-30.
18. G.P. Ivantsov: *Dokl. Akad. Nauk SSSR*, 1947, vol. 58, p. 567.
19. M.J. Aziz: *J. Appl. Phys.*, 1986, vol. 53, pp. 1158-68.
20. M.J. Aziz and T. Kaplan: *Acta Metall.*, 1988, vol. 36, pp. 2335-47.
21. D.S. Kanibolorsky, O.A. Bieloborodova, N.V. Kotava, and V.V. Lisnayak: *J. Ther. Anal. Calor.*, 2003, vol. 71, pp. 583-91.
22. V.E. Zinov'ev, L.D. Zangrebia, L.N. Petrova, and V.A. Sipilor: *Iaevestiya Vysshikh Uchebnykh Zavendeii Fizika*, 1983, vol. 6, pp. 36-41.
23. W.J. Boettinger and S.R. Coriell: in *Science and Technology of Undercooled Melts,* P.R. Sahms, H. Jones, C.M. Adams, eds., Martinus Nijhoff, Dordrecht, The Netherlands, 1986, p. 81.
24. S. Bysakh, S. Mitra, G. Phanikumar, J. Majumdar, P. Dutta, and K. Chattopadhyay: *Metall. Mater. Trans. A*, 2003, vol. 34A, pp. 2621-31.
25. E.A. Brandes: Smithel's reference handbook, 6th ed., Butterworth, London, 1983.
26. R. Trivedi, P. Magnin, and W. Kurz: *Acta Metall. Acta Metall. Mater.*, 1987, vol. 35, pp. 971-80.
27. J.D. Hunt and K.A. Jackson: *Trans. Met. Soc. AIME*, 1966, vol. 236, pp. 1129-42.
28. W. Kurz and R. Trivedi: *Metall. Trans. A*, 1991, vol. 22A, pp. 3051-57.
29. S.R. Corriel and D. Turnbull: *Acta Metall.*, 1982, vol. 30, pp. 2135-39.